

# The first comparison between Swarm-C accelerometer-derived thermospheric densities and physical and empirical model estimates

Timothy Kodikara<sup>1,2</sup>, Brett Carter<sup>1</sup>, Kefei Zhang<sup>1</sup>

<sup>1</sup>SPACE Research Centre, RMIT University, Melbourne, VIC, Australia

<sup>2</sup>SERC Limited, AITC2 Mount Stromlo Observatory, Canberra, ACT, Australia

## Key Points:

- First analysis of Swarm-C accelerometer-derived densities using physical and empirical models
- TIE-GCM and NRLMSISE-00 are used to study the thermosphere at Swarm-C's 10 second temporal resolution during June–December 2014
- TIE-GCM significantly outperforms NRLMSISE-00 and strong indications that TIE-GCM's model-bias is mostly controlled by the parametrization of solar activity.

arXiv:1712.01961v1 [physics.ao-ph] 5 Dec 2017

## Abstract

First systematic comparison between Swarm-C accelerometer-derived thermospheric density against both empirical and physics-based model results using multiple model performance metrics is presented. This comparison is performed at the satellite's high temporal resolution, which provides a meaningful evaluation of the models' fidelity for orbit prediction and other space weather forecasting applications. The comparison against the physical model is influenced by the specification of the lower atmospheric forcing, the high-latitude ionospheric plasma convection and solar activity. A machine-learning exercise is also used to isolate the impact of thermosphere-driving mechanisms. The results show that the short-timescale variations observed by Swarm-C during periods of high solar and geomagnetic activity were better captured by the physics-based model as compared to the empirical model in this analysis. It is concluded that Swarm-C data agree well with the climatologies inherent within the models, and is therefore a useful dataset for further model validation and scientific research.

## 1 Introduction

The response of neutral mass density in the thermosphere (hereinafter density) to various space weather conditions is not well understood. Density is one of the most significant uncertainties in tracking and predicting the orbit of a space object in low Earth orbit (LEO) [Vallado, 2004; Vallado and Finkleman, 2014; Bennett *et al.*, 2015]. Precise knowledge of the variations in density is also critical for attitude control, predicting satellite lifetime and re-entry point as well as collision avoidance maneuvers in LEO [Vallado, 2004]. The only way to predict density in space and time is through modeling, ergo the uncertainty in model estimates limits our ability to assure the safety of operational satellites [Zesta and Huang, 2016].

Various techniques to estimate density exist and have been appraised in many studies [e.g., Emmert, 2015]. Empirical models of density are based on climatologies derived from observations. Although most widely used in orbit tracking and prediction exercises, empirical models are limited in their resolution especially at short timescales mainly due to the averaging and scarcity of observations [Emmert, 2015]. Physical models numerically solve the fluid equations to derive evolving thermospheric parameters such as density, temperature, winds and composition [Qian and Solomon, 2012]. Capturing the evolving thermospheric responses are critical for a forecast model. For example, as noted in Lin *et al.* [2013], satellite tracking errors at 400 km during even moderate magnetic storms are about 65% greater than at quiet times. Looking at the growth and resilience regarding nowcast and forecast capabilities in physical models of terrestrial weather, atmospheric researchers are sanguine about similar prospects for physics-based upper-atmospheric models [Chen *et al.*, 2011].

Two main drivers of density are the solar irradiance and the geomagnetic activity [Knipp *et al.*, 2004]. In modeling the contribution of these drivers, both physics-based Thermosphere-Ionosphere-Electrodynamics General Circulation Model (TIE-GCM) (see Section 2.1) and the empirical Mass Spectrometer Incoherent Scatter Radar Model (NRLMSISE-00) (see Section 2.2) use  $F_{10.7}$  (see Tapping [2013]) as a proxy to the solar irradiance and  $Kp$  and  $Ap$  indices (see Menvielle and Berthelier [1991]) respectively to represent the geomagnetic activity. Also, internal mechanisms originating from the lower atmosphere, such as tides, turbulence and planetary waves, dissipate energy into the ionosphere-thermosphere system and thus change its thermal, dynamical, and compositional structure [Liu, 2016]. At the TIE-GCM's lower boundary an empirical formulation representing the seasonal variations in the advective and diffusive transport of primarily atomic oxygen is imposed [Qian *et al.*, 2009]. While this representation of lower atmospheric disturbances (collectively referred to as eddy diffusion ( $K_{zz}$ )) showed an improvement in Qian *et al.* [2009], it also engendered undesired problems in Siskind *et al.* [2014] and Jones *et al.* [2017] as  $K_{zz}$  attempts to contain both short wavelength eddies and, larger dynamical and diffusive processes.

Codrescu *et al.* [2008] compared the impact of  $F_{10.7}$  and  $Kp$  on thermospheric temperature using the physics-based CTIPE model (see Fuller-Rowell and Rees [1980]) and the

MSIS-86 model, which is an earlier version of the NRLMSISE-00, and concluded that the temperature variation due to  $F_{10.7}$  in the MSIS-86 model is unrelated to the season and geomagnetic activity. Although the time-of-day dependency on the model performance was small in *Codrescu et al.* [2008], the temperature variation due to  $F_{10.7}$  in the CTIPE model was influenced by both season and geomagnetic activity. Navier-Stokes equations applied to the thermosphere relates that density depends on the temperature profile as well as the compositional structure of ions and neutrals. Moreover, *Masutti et al.* [2016] showed that the density bias in the physics-based GITM model (see *Ridley et al.* [2006]) compared to CHAMP (Challenging Minisatellite Payload) and GRACE (Gravity Recovery and Climate Experiment) accelerometer-derived densities, linearly increases with  $F_{10.7}$ . Such a linearly increasing bias with  $F_{10.7}$  has not been reported for TIE-GCM. *Emmert et al.* [2014] provides a comparison of average density change during two consecutive solar minima due to  $F_{10.7}$  and  $Kp$  in NRLMSISE-00 and TIE-GCM version 1.94.2 with respect to a statistical formulation in the Global Average Mass Density Model. *Emmert et al.* [2014]’s study concluded that the effect attributable to  $F_{10.7}$  and  $Kp$  is not significantly different for both models, NRLMSISE-00 and TIE-GCM, under quiet conditions. Rather than using the  $F_{10.7}$ , *Solomon et al.* [2011], using the MgII core-to-wing ratio as the solar EUV proxy to TIE-GCM version 1.93 showed that EUV effect on density change under solar-minimum conditions is significantly higher than that of the geomagnetic activity.

*Siemes et al.* [2016] showed the good correspondence between calibrated Swarm-C density and, solar and geomagnetic activity indicating the suitability of the data for detailed investigations. Swarm-C satellite (see *Friis-Christensen et al.* [2008]) is equipped with eight channels of GPS trackers. The GPS signals combined with precise orbit determination (POD) techniques are used to calibrate and validate the accelerometer data. *Xiong et al.* [2016] reports on the events of total loss of GPS signal that have in turn made the accelerometer data during those events less reliable. *Siemes et al.* [2016] reports that drag calculations from POD are not sufficiently optimized for the Swarm constellation. The task of extracting the pure non-gravitational signal from the raw accelerometer measurements is discussed in *Siemes et al.* [2016]. *Bezdek et al.* [2017] provides a comparison between these raw measurements and modeled non-gravitational accelerations based on NRLMSISE-00 derived densities. Yet, to our knowledge, accelerometer-derived densities from the Swarm-C has not been used so far as a viable model validation data-set.

In most of these model performance analyses, the model estimates and data are normalized to a nominal altitude [e.g., *Emmert et al.*, 2014; *Elvidge et al.*, 2016]. The biases induced by the normalization technique is cancelled out when both data and model estimates are treated equally. Therefore, normalization allows to simplify the comparison and is rather suitable for a comparison of the average behavior of model and data. As noted in *Elvidge et al.* [2014], assessing model performance using just one metric (typically difference or ratio between model and data) may hide other underlying biases of the model. Furthermore, when comparing long-term density with for example solar or geomagnetic activity, data/model ratio provides a better visualization of the correlation than the residual as the seasonal, semi-annual amplitude difference of density is relatively higher than that of solar and geomagnetic activity. A comparison along each epoch, on the other hand, may provide a more robust test of the ability of a forecast model to describe the high-resolution temporal and spatial variations.

In this study, the model performance is analyzed at the Swarm-C’s spatial and temporal resolution by using five different metrics. This paper provides a useful validation of the new Swarm-C data and shows the valuable addition it makes to the existing density-database, which is sparse compared to other regions of the atmosphere. The paper also discusses the effect of driving NRLMSISE-00 with the indicated full history of  $Ap$  and the daily average  $Ap$  under solar-maximum conditions. The impact of space weather parameterization ( $F_{10.7}$  and  $Kp$ ) in TIE-GCM is investigated from various aspects. The impact of  $K_{zz}$  on density is studied using the latest version of TIE-GCM along with a comparison of two high-latitude empirical ion convection models. Furthermore, utilizing a machine-learning cross-validation

scheme, how the systematic bias due to space weather parameterization affects model performance is studied.

## 2 Models and Data

The study presented here corresponds to the period June–December 2014, which is the solar-maximum year with the lowest recorded solar activity in over 100 years since regular record keeping began circa 1750 [Hathaway, 2015]. A brief description of the Swarm-C data and the two models used in the comparison is provided below.

### 2.1 Thermosphere-Ionosphere-Electrodynamics General Circulation Model

TIE-GCM is a three-dimensional, time-dependent, physical model of the upper atmosphere [Dickinson *et al.*, 1981; Richmond *et al.*, 1992]. TIE-GCM assumes a constant acceleration due to gravity ( $870 \text{ cm/s}^2$ ) and spherical symmetry of the Earth. This study employs the two most recent versions of the TIE-GCM: 1.95 and 2.0. The latest version distinguishes argon as a minor constituent and helium as a major constituent. The helium concentration can have a significant impact on atmospheric drag calculations, especially under solar-minimum conditions [Sutton *et al.*, 2015]. Version 2.0 also allows the option to specify a background zonal mean climatology of winds and temperature at the lower boundary—default flat conditions are used in our model runs.

The model runs are performed on a  $5^\circ \times 5^\circ$  grid in latitude and longitude along 29 isobaric layers that extend from approximately 97–600 km in altitude. The isobaric layers are separated by  $0.5 H$ , where  $H$  is the scale-height of the constituents. Lower boundary wave forcing is specified through numerically derived migrating diurnal and semi-diurnal tides [see Hagan *et al.*, 1999].

TIE-GCM is capable of accepting magnetospheric inputs from multiple sources and methods, such as assimilating direct observations and coupling with empirical or numerical models. The inputs required are the high latitude ion convection, Hemisphere Power (HP), and the Cross Polar Cap Potential (CPCP). High-latitude ion convection patterns derived from the electric potential model of Weimer [2005] (hereinafter TIE-GCM(W)) and the Heelis *et al.* [1982] ionosphere convection model (hereinafter TIE-GCM(H)) are utilized separately in the model runs presented here. High latitude auroral precipitation is determined through  $Kp$ -dependent HP and CPCP. The Heelis *et al.* [1982] empirical model depends on the CPCP and the strength and direction of the interplanetary magnetic field (IMF). In addition to IMF strength and direction, the Weimer [2005] model depends on the dynamics of the solar wind, and the orientation of the geomagnetic dipole.

The thermosphere-ionosphere coupling with the plasmasphere is described by the direction of flow of plasma flux at the upper boundary. The EUVAC solar proxy model of Richards *et al.* [1994], with modifications by Solomon and Qian [2005], is used as the solar heat input throughout all the TIE-GCM simulations presented here. In the EUVAC model, solar heating is described by the  $P$  index, which is a solar flux average based on the daily  $F_{10.7}$  and its running 81-day-centered mean that can be mathematically expressed as,

$$P(i) = \frac{1}{2N+1} \sum_{j=-N}^N F_{10.7}(i+j), \quad (1)$$

where  $i$  is the day-of-year the model is evaluated for and  $N$  is 40.

Each TIE-GCM simulation was primed with an arbitrarily chosen 15-day "settle-in" period and only the model outputs after this period are considered here.

### 2.2 Mass Spectrometer Incoherent Scatter Radar Model

Picone *et al.* [2002] introduced the NRLMSISE-00 empirical model as a significantly modified version of the original MSIS-class models: MSIS-86 and MSIS-90 [see Hedin,

1987; *Hedin et al.*, 1991]. The NRLMSISE-00 model describes the atmosphere from ground level to the exosphere and is based on data from satellites, rockets, and radars over several decades [*Picone et al.*, 2002]. The model uses curve fitting techniques to estimate the temperature, composition and density for a given altitude, latitude, longitude, universal time, 81-day centered-mean  $F_{10.7}$ , daily  $F_{10.7}$ ,  $A_p$  geomagnetic indices for seven periods of anterior magnetic activity, and apparent local solar time.

One significant addition in the NRLMSISE-00 is the accounting of anomalous oxygen ( $O^+$ ) in the calculation of density for altitudes beyond 500 km. Similar to most other upper atmospheric models, including TIE-GCM, the NRLMSISE-00 model assumes spherical symmetry of the Earth, however, unlike TIE-GCM, it uses spherical harmonics to resolve for the grid positions to map the model outputs. In the NRLMSISE-00 model, the thermospheric outputs mainly depend on exospheric temperature profile for which the *Walker* [1965] temperature profile is used with certain modifications to the EUV contribution introduced by *Picone et al.* [2002].

### 2.3 Swarm-C Accelerometer-derived Neutral Density

Swarm, launched in late 2013, consists of three near-polar (angle of inclination:  $84.7^\circ$ – $88^\circ$ ) satellites designed for monitoring the magnetic field of the Earth. The satellites also carry accelerometers and GPS receivers on board—measurements used to derive the density [*Siemes et al.*, 2016].

By October 2017, only the Swarm-C (average orbital height, 480 km) post-processed density product was available. The Swarm-C density product is subject to several disturbances and is not yet fully optimized to account for all variants of non-gravitational accelerations [*Siemes et al.*, 2016]. In the Swarm constellation, only Swarm-C has been identified as the least affected by these disturbances. Only the linear acceleration (in-track) during the period 02 June–31 December 2014 has been considered in the density product used in this study. It is expected that as the Swarm satellites gradually decay in orbital height; the higher non-gravitational acceleration signal may help improve the calibration of accelerometer-derived densities.

## 3 Methods

The physics-based TIE-GCM and the empirical NRLMSISE-00 models were used in different configurations to estimate the densities along the Swarm-C orbit. The ensemble of model runs is listed below.

#### TIE-GCM Runs:

1. **T1** TIE-GCM(H)-version 2.0 with day-of-year dependent  $K_{zz}$  coefficient.
2. **T2** TIE-GCM(H)-version 2.0 with constant  $K_{zz}$  coefficient.
3. **T3** TIE-GCM(W)-version 2.0 with constant  $K_{zz}$  coefficient.
4. **V1** TIE-GCM(H)-version 1.95 with constant  $K_{zz}$  coefficient.

#### NRLMSISE-00 Runs:

5. **M1** NRLMSISE-00 driven with the full required history of  $A_p$ .
6. **M2** Similar to M1 but with a daily average of 3-hour  $A_p$ .
7. **M3** Similar to M1 but with  $O^+$  added to the density.
8. **M4** Similar to M2 but with  $O^+$  added to the density.

Through runs 1–4, the effect of different configurations of empirical high-latitude potential models coupled to the TIE-GCM, and  $K_{zz}$  coefficient on density is investigated. Through runs 5–8, the effect of accounting for empirically estimated  $O^+$ , and geomagnetic activity expressed as daily average or a combination of anterior magnetic activity up to 56 hours on density is studied using the NRLMSISE-00 model.

The cubic spline interpolation scheme was used to map the TIE-GCM estimated densities along the satellite orbit, first along the latitude and longitude and then vertically to the satellite altitude. Normalizing the Swarm-C densities to a specific altitude was omitted to rid the data from interpolation biases and gain an opportunity to compare the models' performance at the satellite altitude, which is an important attribute in applications of orbit determination and orbit prediction. NRLMSISE-00 densities were estimated by passing the satellite coordinates to the model for each epoch serially.

Model-bias in upper atmospheric density modeling is often assessed by different metrics, such as root-mean-square-error (RMSE), standard deviation, absolute difference, model/observation ratio, log-normal ratio or a combination thereof [e.g., *Doornbos, 2012; Elvidge et al., 2014*]. The upper atmospheric density assumes a log-normal distribution and also exhibits approximate characteristics of a Gaussian (normal) distribution [*Bezdek, 2007*]. However, the non-linear error sources in data/model alter the log-normal mean of the distributions. Therefore, using the Gaussian standard deviation to assess model-bias/ratios can often lead to ambiguous interpretations due to the Gaussian scaling required in such comparisons [*Doornbos, 2012*]. Overall, there is no one standard test to determine the best model.

Therefore, in this study, the models' performance is evaluated on several metrics: difference in density ( $\rho_{\text{diff}} = \rho_m - \rho_o$ ), density ratio ( $\rho_{\text{ratio}} = \rho_o / \rho_m$ ), the standard deviation  $\sigma$ , Pearson correlation coefficient  $R$ , model-bias  $B$  and the error-standard deviation  $E$ . Subscripts  $o$  and  $m$  represent Swarm-C data and model estimated values respectively.  $\rho_{\text{ratio}} = 1$  would indicate that the two density values/distributions are identical. Density ratio limits the range of values when looking at the difference between the estimated density and the observed density and also allows to highlight the magnitude of the proportional difference in a more straightforward manner.

Model-bias and model error-standard deviation is defined similarly to *Elvidge et al. [2014]*,

$$B = \bar{m} - \bar{o}. \quad (2)$$

Equation (2) gives the  $B$  as the difference between the mean of model estimates ( $\bar{m}$ ) and mean of observations ( $\bar{o}$ ). The  $E$ , which is also sometimes referred to as the centered-pattern root-mean-square difference is calculated as,

$$E = \sqrt{\sigma_m^2 + \sigma_o^2 - 2\sigma_m\sigma_o R}. \quad (3)$$

The use of  $E$  as a measure of model variation is useful especially in comparing distributions that are usually strongly correlated. However, strong correlation does not imply the two distributions share the same amplitude of variation. The construction of  $E$  that is linked to the standard deviations of the two distributions  $m$  and  $o$ , allows the distinction of the differences in the amplitude variation of the distributions. If two distributions are identical,  $E$  will be zero. A positive  $E$  value indicates the tendency of the model to estimate higher than the mean of observations and a negative  $E$  value indicates the opposite.  $E$  is different from the root-mean-square difference that is commonly used in literature where the two will only be equal if the model (distribution/pattern) that is compared has zero bias with respect to the truth/observations as  $E$  is the root-mean-square difference sans the mean [*Taylor, 2001; Elvidge et al., 2014*]. This method is, however, limited to evaluate only the sampling variability in the model and not in the observations. The uncertainty in observations used here are set at naught.

For a deeper investigation of the impact  $Kp$  and  $F_{10.7}$  (space weather parameters) impacts on density estimates, a machine learning cross-validation model based on *Pedregosa et al. [2011]* was built. The cross-validation scheme attempts to predict the variability in a portion of the density distribution (validation set) by learning the response of density to space weather parameters in another portion of the respective distributions (training set). In this experiment, the entire time-series was split into 100 parts and iterated over 100 times giving 99 training sets and one validation set for each prediction step. The folding value 100 to split the dataset was empirically chosen as smaller or larger folding value turned out to be

non-optimal. The average of the resulting RMSE is considered in the results shown below. Note that these are the RMSE of the predicted values from the cross-validation scheme and not the RMSE for the different distributions compared as a whole. While each model has its way of calibrating space weather parameters, this test allows us to recognize the amount of relative influence each of the space weather parameters has on the observed variation in density.

#### 4 Results

Figure 1 shows the solar and geomagnetic activity and the Swarm-C accelerometer-derived density during June to December 2014. The daily average of the Swarm-C accelerometer-derived density (black),  $P$  index (blue),  $F_{10.7}$  (magenta) and the EUV flux (green) are shown in Figure 1a. Figure 1b shows the hourly average of the Swarm-C accelerometer-derived density (black) and the 3-hour geomagnetic activity  $Kp$  (red). Figures 1c and d display the daily averages of  $\rho_{\text{ratio}}$  and  $\rho_{\text{diff}}$  for T1 (blue), T2 (green), T3 (yellow), V1 (purple), M1 (magenta) and M2 (grey) model-data comparisons respectively. The gaps in the line-graphs in Figure 1 mark the data gaps in the Swarm-C data, 23 October–02 November, 30 November–03 December, and 21–22 December 2014. The last data gap is less than 24 hours and therefore is not reflected in the daily averaged graphs.

Figure 1a shows the good correspondence of the Swarm-C data with the solar flux variations. Whilst the variations of all three solar activity indicators are quite similar; there are some subtle differences. For example the smooth EUV variations relative to the  $P$  and  $F_{10.7}$  from September onwards. In Figure 1b, the higher-frequency variations in the hourly averaged Swarm density data show some similarities to the variations in the  $Kp$ ; e.g., in late August and mid-September. Interestingly, the variations in  $\rho_{\text{ratio}}$  in Figure 1c and  $\rho_{\text{diff}}$  in Figure 1d also seem to reflect the solar activity variations in Figure 1a and the geomagnetic activity variations in Figure 1b. For example, the crest and trough locations in  $\rho_{\text{ratio}}$  and the solar indices during July, as well as the sudden variations in  $\rho_{\text{ratio}}$  and  $\rho_{\text{diff}}$  in late August, coincide with significant changes in the  $Kp$ .

When comparing the performance of the individual model runs to the Swarm-C data in Figure 1, it can be observed that prior to September, the T1 run performed the best with  $\rho_{\text{ratio}}$  close to 1 and the smallest overall values for  $\rho_{\text{diff}}$ . However, from September onwards, the T2, T3, and V1 runs typically outperform the T1, M1, and M2 runs.

The gradual transition from the mid-year semi-annual minimum to maximum in density is also visible in Figure 1a where the density in December is double on average compared to June.

Figures 2a and b summarize the statistical results of the comparisons between the model runs and the Swarm-C data for all epochs and the daily averaged Swarm-C data, respectively. The low-order statistics displayed in Figure 2 in a modified-Taylor diagram (MTD) are the  $\sigma$ ,  $R$ ,  $E$ , and  $B$  [Taylor, 2001; Elvidge *et al.*, 2014]. The black star labeled "Swarm-C" indicates the bias-free hypothetical truth-point to which the models are referenced. At this point,  $\sigma$  equals the normalizing factor,  $R$  equals 1, and  $E$  equals 0. The radial distance from the origin indicates the  $\sigma$ , normalized to the standard deviation of the Swarm-C data (black dashed line).  $R$  is delineated on the outer edge of the standard deviation arc. The dot marking the model's position on the diagram also represents the normalized  $B$  given in the color bar underneath.  $B$  is calculated as per Equation (2). The blue-dotted arc indicates  $E$  as per Equation (3). The absolute values for  $\sigma$ ,  $E$ , and  $B$  are obtained by multiplying by the normalization factors  $4.30 \times 10^{-16} \text{ g/cm}^3$  and  $3.22 \times 10^{-16} \text{ g/cm}^3$  for Figures 2a and b, respectively.

Figure 2 shows that comparing model performance for averaged values versus per each epoch leads one to draw different conclusions about the models' performance. However, it is clear that TIE-GCM outperforms NRLMSISE-00 in all four metrics in both data comparisons. The complete statistics corresponding to all eight runs are given in Appendix A.1. A noteworthy result of Figure 2 is that applying a temporal average on the data (i.e., taking the

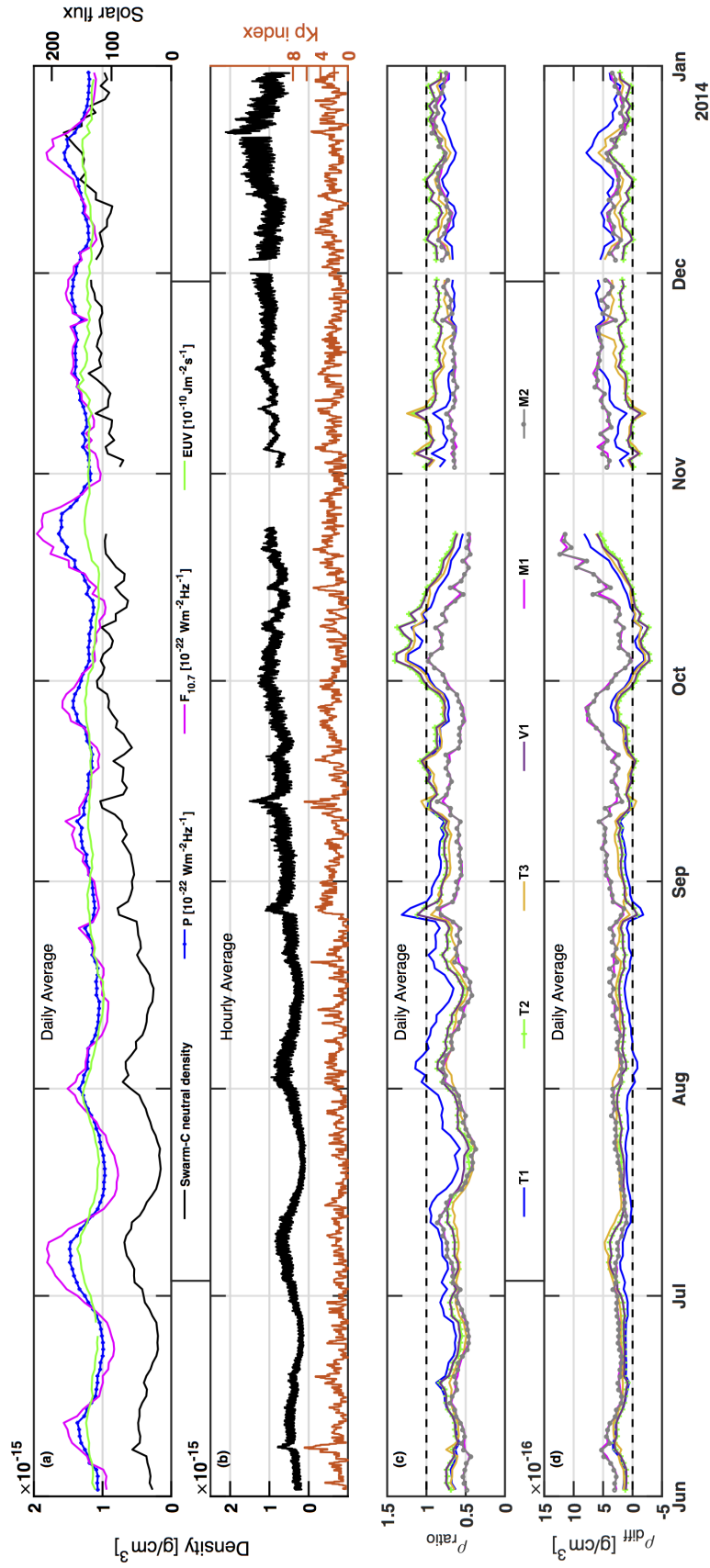


**Figure 1.** (a) Daily average of Swarm-C accelerometer-derived density,  $F_{10.7}$ ,  $P$  index and EUV flux density. (b) Hourly average of Swarm-C data and the 3-hourly  $Kp$ . (c) Daily average of density ratio ( $\rho_{\text{ratio}}$ ) for six of the model runs considered in the study. T1, T2, T3 and V1 are simulations using the TIE-GCM and, M1 and M2 are the NRLMSISE-00 model runs. (d) Same as (c), but for the difference in density ( $\rho_{\text{diff}}$ )

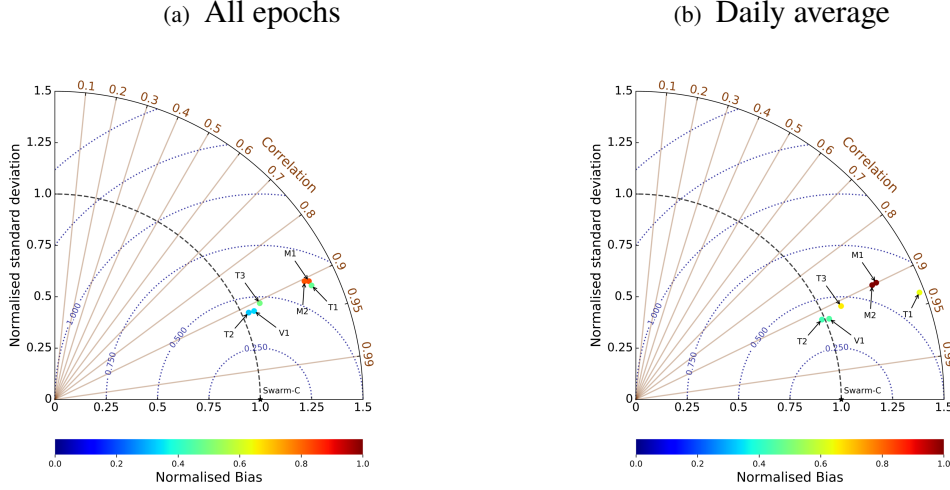


**Figure 2.** Modified-Taylor digram [Elvidge *et al.*, 2014] showing the low-order statistics for the six model scenarios introduced in Figure 1. The bias-free reference point is labeled as Swarm-C. The locus from the origin (0,0) bears the normalized standard deviation. The angle subtended by the standard deviation arc represents the correlation coefficient. The blue-dotted arc indicates the model error-standard deviation. The model-bias is shown on the color scale. The normalizing factors used to scale each of these statistical parameters are (a)  $4.30 \times 10^{-16} \text{ g/cm}^3$  and (b)  $3.22 \times 10^{-16} \text{ g/cm}^3$  considering all valid satellite epochs and the daily average of the distributions respectively.

daily average of the 10-sec Swarm-C data) does not appear to affect the models' position on the MTD chart, with the exception of T1 that has an increase in the normalized bias and the standard deviation.

It can be seen that both NRLMSISE-00 and TIE-GCM are positively biased—a tendency Elvidge *et al.* [2016] also observed in a study comparing the two models to CHAMP accelerometer-derived densities. On the one hand, averaging out increases the correlation coefficient for the physics-based models, but has a minimal negative impact on the empirical model. On the other hand, averaging out improves the standard deviation for all the model runs. As a result of lower standard deviation, the model error-standard deviation is improved in Figure 2a compared to Figure 2b.

Overall, the results in Figure 2 shows that the T2 and V1 runs that employ a constant  $K_{zz}$  coefficient have the closest resemblance to the Swarm-C accelerometer-derived density—the highest correlations and smallest model error standard deviations. Interestingly, the T1 run, which employed a seasonally varying  $K_{zz}$  coefficient, performed significantly worse in terms of the model error standard deviation. The statistical results from the M1, M2, M3 and M4 runs are all very similar to each other, indicating that the different NRLMSISE-00 runs had a little overall impact on their comparisons against the Swarm-C data.

A clear correlation between  $\rho_{\text{ratio}}$  and  $\rho_{\text{diff}}$  to geomagnetic and solar activity is apparent in Figure 1. To further investigate this impact, Figure 3 presents a composite of bivariate distributions of the hourly averaged  $\rho_{\text{ratio}}$  and  $\rho_{\text{diff}}$  as functions of the  $Kp$  and  $F_{10.7}$ . The vertical axes in the panels of Figure 3a and b show the density ratio as the deviation from the ideal ( $\rho_{\text{ratio}} - 1$ ) and the  $\rho_{\text{diff}}$  respectively, for each model run. The positive and negative values on the vertical axes indicate the model overestimate and underestimate, respectively. The green dots show the scatter distribution while the contour lines are drawn in the order of increasing color-intensity to display the bivariate probability density distribution. The separation of contour lines is directly related to the mean integrated squared error, which is used for the estimation of the bandwidth for the kernel density. The linear regression fit is shown by

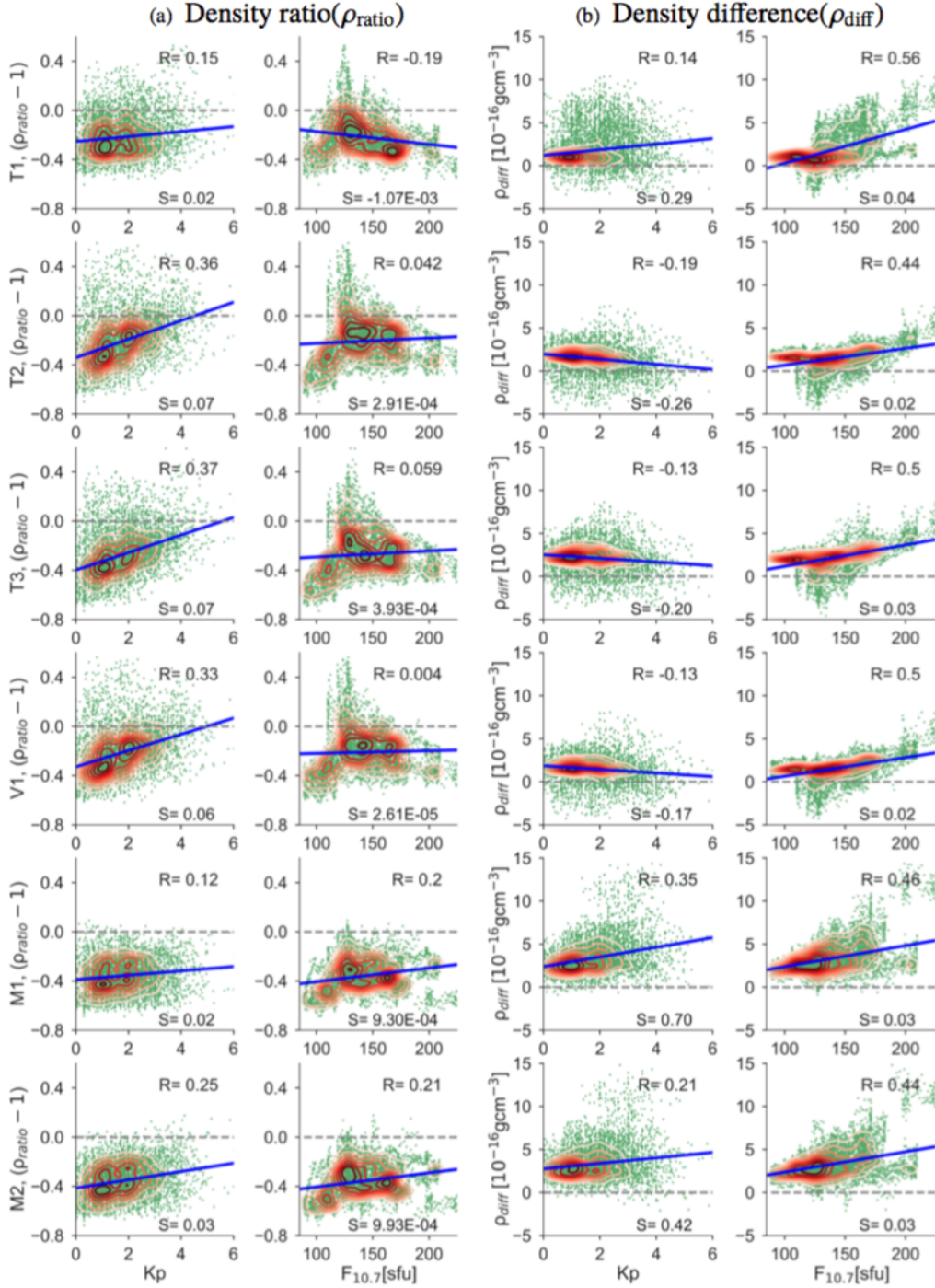


**Figure 3.** The correlation of the  $Kp$  index and the  $F_{10.7}$  solar flux with the hourly averaged (a)  $\rho_{\text{ratio}}$  and (b)  $\rho_{\text{diff}}$ .  $\rho_{\text{ratio}}$  is displayed as the deviation from the ideal. The simulation corresponding to each row is labeled on the left most column, which are the same as in Figure 1. The green dots show the scatter distribution while the contour lines represent the bivariate probability density distribution. The blue line indicates the linear regression fit and slope of the line is displayed as  $S$ . The Pearson correlation coefficient is displayed as  $R$ . The broken line provides the comparable Swarm-C reference.

the blue-line, and its slope is displayed as  $S$ . The Pearson correlation coefficient is displayed as  $R$ .

Figure 3a demonstrates a linear increase in the  $\rho_{\text{ratio}}$  with increasing  $Kp$ . A similar tendency is seen in relation to increasing  $F_{10.7}$  except for T1, where the trend is negative. However,  $R$  pertaining to the  $F_{10.7}$  is 1–2 orders of magnitude less compared to that of the  $Kp$  distribution, except for T1 and the M1–M4 runs. Furthermore, the corresponding slope of the linear regression fit is minimal in the  $F_{10.7}$  column.

The  $Kp$  column in Figure 3b shows that T2, T3 and V1 runs have an improvement in performance with increasing  $Kp$  ( $\rho_{\text{diff}} \rightarrow 0$ ), whereas the other runs indicate a positive correlation out of which M1 has the highest correlation coefficient ( $R = 0.35$ ). Yet, unlike the comparison with  $\rho_{\text{ratio}}$ , the  $\rho_{\text{diff}}$  shows a striking correlation to  $F_{10.7}$  with a significantly higher slope and correlation coefficient. This linear relationship indicating that model performance degrades with increasing  $F_{10.7}$  may be somewhat exaggerated because the magnitude of the density in the thermosphere system is increased in general during high solar activity.

Comparing  $F_{10.7}$  with  $\rho_{\text{ratio}}$  provides a synthesized view of the model performance with respect to the solar activity. A notable distinction between the T1 run and the other three TIE-GCM runs is apparent in Figure 3. The distinction connotes the control that variable eddy diffusivity imparts on space weather forcing ( $Kp$  and  $F_{10.7}$ ) in the physics-based model. Interestingly, two primary clusters in the scatter distribution are common among all runs in the  $F_{10.7}$  column in Figure 3: the small contour lines near 200 sfu and the large cluster to the left ( $<170$  sfu). It can be seen from  $F_{10.7}$  versus  $\rho_{\text{ratio}}$  that better  $\rho_{\text{ratio}}$  is recorded between  $\sim 120$  and  $150$  sfu for the physics-based model and that T1–3, and V1 runs perform poorly at the two extremes of  $F_{10.7}$  given in the figure. Although the empirical model is more stable than the TIE-GCM in the range  $\sim 120$ – $150$  sfu and demonstrates a slight improvement near 200 sfu, its relative difference is higher than the physics-based model. In addition, the NRLMSISE-00 runs in Figure 3, demonstrate a consistent positive correlation to both  $Kp$  and  $F_{10.7}$ .

Furthermore, in Figure 3a– $F_{10.7}$ , all TIE-GCM runs share a triangular shaped scatter distribution, which is not common for the empirical model. This pattern has a significance in scatter-distributions in which the correlations can be investigated in three important regions. A very pronounced linear relationship can be drawn from the minimum  $F_{10.7}$  to the centre of the scatter distribution. The geometry in the middle region near 120 sfu indicates an uncorrelated or random distribution of density ratio. A negative correlation is apparent from the center to the right of the  $F_{10.7}$  distribution. Similar uncorrelated geometries can also be observed in the corresponding panel in Figure 3b. Figure 4(top) shows the deviation of density ratio from the ideal ( $\rho_{\text{ratio}} = 1$ ) for a given level of solar and geomagnetic activity. Figure 4(bottom) provides a similar comparison for the  $\rho_{\text{diff}}$ . The model run corresponding to each column a–f in Figure 4 is labeled at the top. Both color scales are centered at zero, where the positive and negative values indicate the model overestimate and underestimate, respectively. The representation in Figure 4 is derived by forming  $Kp$  from 0–7 and  $F_{10.7}$  from 80–220 sfu into an  $8 \times 8$  matrix of equal bin-size where the average of each bin is taken as the representative value. The underlying data set corresponds to the hourly averaged densities.

It is clear from both panels in Figure 4 that the physics-based model outperforms the empirical model almost at all levels of solar and geomagnetic activity. TIE-GCM's tendency to overestimate density at higher  $Kp$  and moderate  $F_{10.7}$  ( $\sim 110$ – $135$  sfu) that was apparent in Figure 3 is further accentuated in this figure. That tendency, however, is somewhat subdued by the exclusion of day-of-year dependent  $K_{zz}$ . It is understandable that NRLMSISE-00 experiences a performance degradation at high  $Kp$  and high  $F_{10.7}$ . The density of data points belonging to each bin are not equal throughout and much less in the two extremes (high and low  $Kp$  and  $F_{10.7}$ ) than in between.

For a deeper investigation of the impact  $Kp$  and  $F_{10.7}$  imparts on density estimates, a machine-learning algorithm that peruses the data at various intervals and yields the RMSE value based on the predictions it makes was built. The process is carried out by forcing predictions entirely based on  $Kp$  and  $F_{10.7}$  (referred to as "feature" distributions in the machine-

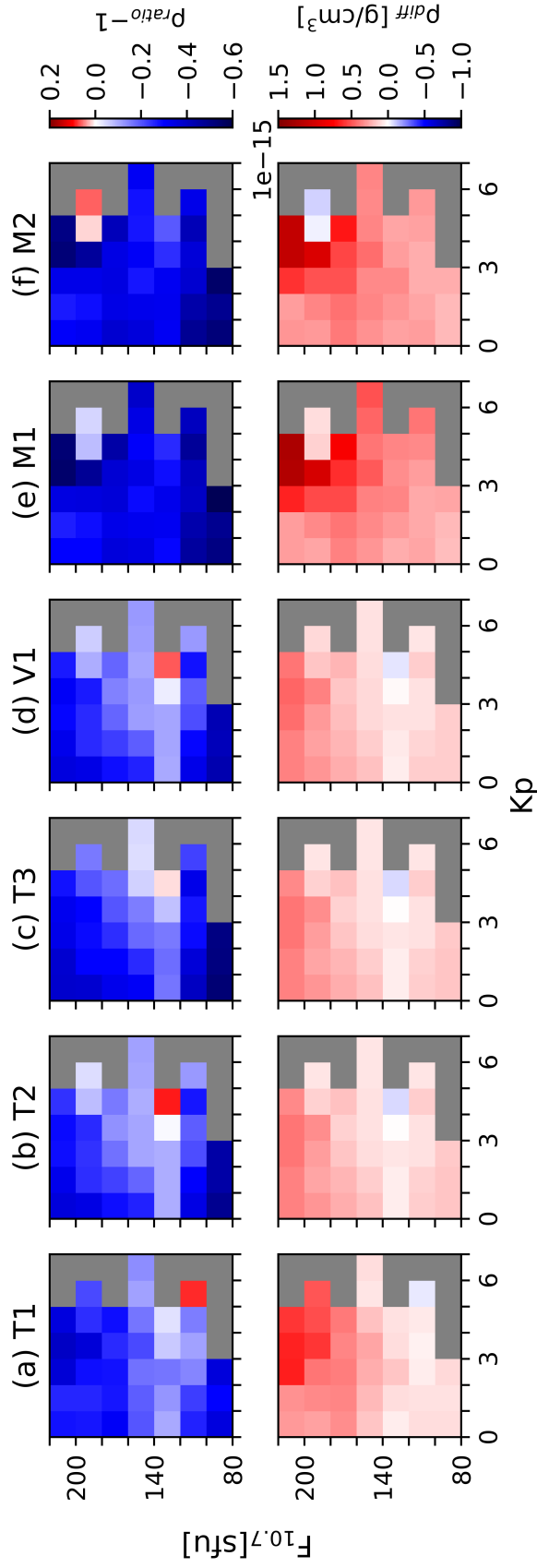


**Figure 4.** The density ratio and density difference averaged into bins based on solar and geomagnetic activity. Column labels are for the different model runs. The respective color-scales represent the average of each bin.

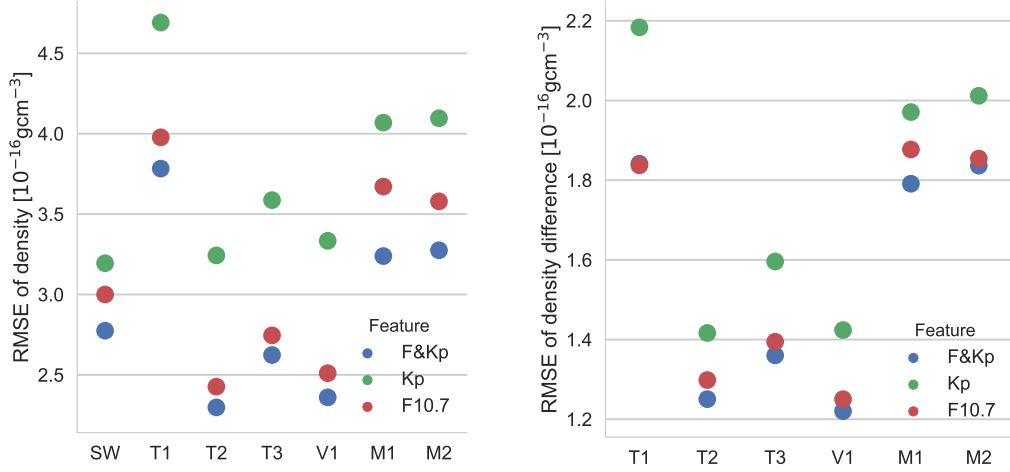


**Figure 5.** 1-D graph for the root-mean-square-error results from the machine learning cross-validation scheme. (left) Compared with the different density distributions. SW is for the Swarm-C accelerometer-derived density and other column labels are for the different model runs. (right) Compared with the  $\rho_{\text{diff}}$ . Feature labels represent the distribution used in the training. F10.7 and Kp correspond to predictions made by using  $F_{10.7}$  and  $Kp$  distributions independently and F&Kp is when both  $F_{10.7}$  and  $Kp$  are used together in the training.

learning parlance), taking each into account separately and together. The results are shown in Figure 5.

Figure 5(left) shows the results from the machine-learning cross-validation scheme for the hourly averaged density distributions including the Swarm-C accelerometer-derived density displayed as SW. The results for the  $\rho_{\text{diff}}$  is shown in Figure 5(right). The respective RMSE is color-coded and labeled as "Feature", based on the distribution used in the training dataset.

In Figure 5(left), the column representing the Swarm-C data (SW), which can be regarded as the true density, indicates that the RMSE when only the  $Kp$  is featured is about twice as large when only the  $F_{10.7}$  is featured in reference to the F&Kp. Interestingly, a similar response is seen in the M1 run that is driven with the complete history of geomagnetic activity required by the model. In other words, although the RMSE values are relatively higher for the M1 run, the relative differences in the ratio between the two features Kp and F10.7 are almost identical. This similarity, in turn, provides a counter-validation of the Swarm-C accelerometer data set. In other words, it is suitable for model-data comparative analyses, as it is known that NRLMSISE-00's parameterization of density is based on abundantly validated data.

It is also clear in Figure 5(left) that when just the  $Kp$  distribution is used in the training, the RMSE is relatively high. However, as expected, when both distributions are featured in the training set the RMSE is significantly improved. This is essentially another way of visualizing what is abundantly clear in nature—solar heating is the main driver of density. Therefore, the predictions made solely based on  $F_{10.7}$  are relatively close to the predictions made by both features together (F&Kp). Hence it is likely that the machine-learning algorithm attaches more weight to the variations in solar flux distribution in its predictions.

The columns representing the TIE-GCM runs in Figure 5(left) show a marked difference among themselves as well as compared to the other distributions. The significant difference between T1 and the other three TIE-GCM runs that was apparent in the previous figures

is also present in the predicted RMSE values. The most explicit feature among the TIE-GCM runs is the relative proximity of predictions based on  $F_{10.7}$  to that of F&Kp.

Similarly, the RMSE of the  $\rho_{\text{diff}}$  too can be analyzed as shown in Figure 5(right). The relative distance of the green dots from their corresponding red dots in Figure 5(right), reveals that TIE-GCM's response to variations in the geomagnetic activity is characteristically different compared to that of the empirical model. It can also be deduced that TIE-GCM attaches more weight to variations in  $F_{10.7}$  than on  $Kp$  in its density estimation. Moreover, it is clear from the results corresponding to M2 that when NRLMSISE-00 is driven with just the daily  $Ap$ , the variations in  $F_{10.7}$  become more dominant in predicting the model behaviour. M1 compared to M2 shows a better RMSE when both features F&Kp are combined but further away when just the  $F_{10.7}$  is used. Also, note that in M1 the difference in RMSE when just the  $Kp$  is used is almost doubled compared to  $F_{10.7}$  in reference to the F&Kp. Interestingly, the M2's bias toward  $F_{10.7}$  that was shown in Figure 3 is further accentuated in this graph.

In accord with previous figures, the machine-learning predictions display a vast disparity between runs driven with varying  $K_{zz}$  and constant  $K_{zz}$ . T1 in Figure 5(right), indicates that including  $Kp$  in the training has a minor negative effect. Considering how differently the physics-based model responds to the variations in  $Kp$  compared to the empirical model raises the question of whether this phenomenon is indeed related to parameterization errors inside the models. It is noted that while the effect of geomagnetic activity is averaged globally in NRLMSISE-00, the  $Kp$ 's influence on model-derived parameters in TIE-GCM is non-linear.

## 5 Discussion

It is clear from Figure 1 that while both TIE-GCM and NRLMSISE-00 typically overestimate density compared to Swarm-C data, only TIE-GCM underestimated density in a few instances. Interestingly, those instances also correspond to periods of increased geomagnetic activity. In agreement with *Doornbos* [2012]'s discussion about  $\rho_{\text{diff}}$  and  $\rho_{\text{ratio}}$ , it can be seen that model response at these instances is clearly visualized in Figure 1c more than Figure 1d. For example, NRLMSISE-00  $\rho_{\text{diff}}$  in late October is more than twice compared to June. However,  $\rho_{\text{ratio}}$  for the same reveals that model performance did not change as much indicating the usefulness of  $\rho_{\text{ratio}}$  in model evaluation.

Studying the differences between M1–M4 reveals that NRLMSISE-00's performance seems to be not particularly affected much by the extent of the history of  $Ap$  fed into the model. The differences between the two methods of driving NRLMSISE-00 (e.g., M1 and M2) is anticipated to change with geomagnetic activity and the sunspot cycle due to the effect of geomagnetic activity on density. Therefore, the different methods of driving NRLMSISE-00 may especially impact the results at high latitudes during solar minimum.

When comparing the effect of ion convection pattern used in TIE-GCM, clearly TIE-GCM(H) proves to be more efficient than TIE-GCM(W) during the studied period. These results are not too surprising given that the geomagnetic activity was relatively low. *Wu et al.* [2015] showed that in resolving thermosphere winds, the *Weimer* [2005] model performs better during storm times compared to the *Heelis et al.* [1982] model. T3 in Figure 1a slightly overestimated density than T2 during the only two instances where  $Kp$  exceeded 6 and T3 also shows a slight improvement in comparison to T2 during October.

It is clear from Figure 1a that there are instances where  $P$  and  $F_{10.7}$  demonstrate a trend that is different to EUV; e.g., in November, the downward trend in the two proxies not seen in EUV. It can be easily deduced that the differences in variation between EUV versus  $P$  and  $F_{10.7}$  only become more significant on even smaller timescales. This can result in erroneously resolved energy input to the thermosphere system by the EUVAC solar proxy model inside TIE-GCM [*Solomon and Qian*, 2005]. Further, the machine-learning cross-validation scheme reveals the isolated systematic bias of each model run to space weather parameterization, where  $F_{10.7}$  display a larger control over density estimates of TIE-GCM compared to NRLMSISE-00.

T2 and V1 runs where the only difference is the model version, produced very similar results. Although lack of He is not expected to introduce severe errors in total density at Swarm-C's altitude under solar-maximum conditions, Figure 2 showed that T2 is at least slightly better than V1 indicating the improvements made to the model chemistry have an impact even at this altitude.

Out of the four different TIE-GCM runs, it is evident that the introduction of day-of-year dependent  $K_{zz}$  makes a significant impact on the model estimates. In other words, the inclusion of empirically-derived eddy diffusivity push the model estimates closer to Swarm-C data in months following June solstice and farther away post-September equinox (see T1 in Figure 1). Compared to T1, a significant performance degradation for the runs with constant  $K_{zz}$  happens around July and August (e.g., T2 in Figure 1). The model runs with constant  $K_{zz}$  do not show a strong seasonal dependency on performance. As shown in *Qian et al.* [2009, Figure 10], the constant  $K_{zz}$  performs poorly around July minima and our results show on average, driving TIE-GCM with constant  $K_{zz}$  seems to be more effective in this comparison. Nonetheless, from a modeling perspective, these trends suggest that it is beneficial to include daily varying  $K_{zz}$  in density forecasts during June–September.

Results from the machine-learning cross-validation scheme showed that Swarm-C data display a response similar to the NRLMSISE-00 climatology in terms of  $F_{10.7}$  and  $Kp$  ratio. This agreement with climatologies further improves confidence in the Swarm-C data for scientific studies. However, uncertainty in the Swarm-C data was completely ignored in this study. As *Siemes et al.* [2016] points out, uncertainty in the accelerometer measurements and biases induced due to derivation technique are present in the data. One of the important steps in extracting density in the technique used for Swarm-C is to estimate background winds using the *Drob et al.* [2008] empirical horizontal wind model. *Drob et al.* [2015] highlights the substantial disagreements in *Drob et al.* [2008] compared to observations. The *Drob et al.* [2008] model ignores the vertical winds and only represents geomagnetically quiet conditions ( $Kp < 3$ ). Furthermore, even the improved version of the *Drob et al.* [2008] model lacks solar flux parameterization and among others, there are also issues with describing quiet time high-latitude circulation patterns [*Drob et al.*, 2015].

The errors due to background winds are at least an order of magnitude less in comparison to spacecraft along-track velocity vector [*Doornbos*, 2012]. Therefore, its effect on the derived density product may not be of consequence compared to other more significant errors due to accelerometer calibration. Using physical winds in the accelerometer-density derivation process has not been attempted so far to our best knowledge. Winds resolved by self-consistent physical models may help mitigate some of the fundamental issues inherent in empirical winds. Especially in a nowcast/forecast setting, numerically computed winds will eliminate the dependency on statistically averaged winds during disturbed space weather conditions thereby improving the reliability of the derived density product.

## 6 Summary and Conclusions

The first evaluation of the Swarm-C accelerometer-derived densities using the two latest versions of TIE-GCM and the NRLMSISE-00 model was presented. This extended satellite epoch-wise comparison for a continuous six months, as opposed to studying specific events, proved useful in evaluating the models' fidelity for forecasting applications. TIE-GCM outperforms the NRLMSISE-00 model in almost all the metrics used in the comparison. The use of model/data ratio and difference as comparison metrics is discussed. While models show good agreement with the data in both metrics, ratio is a better performance indicator for comparisons with solar and geomagnetic activity.

The results show the complex interconnectedness of solar activity and geomagnetic activity on model performance in terms of estimating density. The presented work, in general, agrees with earlier work concerning model performance during different levels of solar and geomagnetic activity [e.g., *Solomon et al.*, 2011; *Emmert et al.*, 2014].

The impact of two key boundary conditions: eddy diffusion and ionospheric convection, on TIE-GCM's density estimation was analyzed. TIE-GCM shows a strong bias to

the specification of the lower atmospheric eddy forcing. Model runs corresponding to TIE-GCM(W) performed poorly compared to TIE-GCM(H). However, TIE-GCM(W)'s performance was on par with TIE-GCM(H) around the autumnal equinox.

The sensitivity of NRLMSISE-00 model to the specification of geomagnetic forcing was also analyzed. During the studied period where the overall geomagnetic activity was quiet, driving NRLMSISE-00 with just the daily average of  $A_p$  did not seem to have a contrasting effect compared to driving with 7 histories of anterior magnetic activity. Machine-learning cross-validation scheme isolating the driving mechanisms showed that specifying only the daily average  $A_p$  degrades the model performance almost by half. As shown in Solomon *et al.* [2011], depriving the NRLMSISE-00 of complete geomagnetic history results in larger residuals. Picone *et al.* [2002] notes the model's frailty at high latitudes and high geomagnetic activity due to lack of observational data. The results from this study allude to the fact that the NRLMSISE-00 model does not capture the variations in shorter timescales associated with Swarm-C at high solar and geomagnetic activity.

The cross-validation scheme proved useful in demonstrating characteristics inherent to each model run. It was also used to demonstrate that Swarm-C data is commensurate with climatologies. It is concluded that Swarm-C data are indeed suitable for model validation and scientific study. The model performance evaluation could further be improved if the derivation-noise pertaining to Swarm-C can be provided to the user.

Although TIE-GCM is computationally intensive compared to its empirical counterparts, as evident from the results shown here it has the potential to be utilized in density forecasting applications. In addition to forecasting density itself, physical models can also provide the winds required to derive density from accelerometer data. Nevertheless, it is fundamentally important to identify the discrepancies between model and data. In this regard, state-of-the-art data assimilation techniques equip the self-consistent physical models with "self-healing" capabilities whereby the systematic and inherent model biases are corrected as the forecasting progresses to reflect the changes in the real-world observations. This aspect is particularly important to satellite orbit prediction and collision avoidance in LEO.

## **A: Results From The Model Performance Evaluation**

**Table A.1.** Low-order Statistics for the Ensemble of Model Runs<sup>a</sup>

Run	Std	Std*	$R$	$R^*$	Model-bias	Model-bias*	ErrStd	ErrStd*
T1	5.874E-16	4.750E-16	0.914	0.936	2.028e-16	2.049E-16	2.615E-16	2.076E-16
T2	4.442E-16	3.173E-16	0.913	0.919	1.390E-16	1.396E-16	1.834E-16	1.289E-16
T3	4.734E-16	3.532E-16	0.905	0.910	2.112E-16	2.118E-16	2.014E-16	1.464E-16
V1	4.558E-16	3.282E-16	0.914	0.923	1.450E-16	1.456E-16	1.854E-16	1.280E-16
M1	5.856E-16	4.187E-16	0.906	0.899	3.572E-16	3.574E-16	2.675E-16	1.910E-16
M2	5.776E-16	4.113E-16	0.904	0.900	3.513E-16	3.513E-16	2.640E-16	1.856E-16
M3	5.860E-16	4.187E-16	0.906	0.900	3.578E-16	3.580E-16	2.674E-16	1.909E-16
M4	5.776E-16	4.114E-16	0.904	0.900	3.519E-16	3.519E-16	2.639E-16	1.856E-16

<sup>a</sup>Each Run is as defined in Section 3. Std is the standard deviation.

$R$  is the Pearson correlation and ErrStd is the model error-standard deviation.

Superscript \* indicates the daily average of the corresponding all-epochs distribution.

## Acknowledgments

This research was partially supported by a research scholarship awarded to T. Kodikara by the SERC Limited, Mount Stromlo Observatory, Canberra, Australia. This research was also partially supported by an Australian Research Council Linkage grant (LP160100561) awarded to B. A. Carter and K. Zhang. This research was undertaken with the assistance of resources from the National Computational Infrastructure (NCI), which is supported by the Australian Government.

The European Space Agency is acknowledged for providing the Swarm-C data. The measurements  $Kp$ ,  $Ap$  and  $F_{10.7}$  are obtained from NOAA <<http://www.ngdc.noaa.gov/ngdcinfo/onlineaccess.html>>. The IMF measurements are obtained from the OMNI database <<http://omniweb.gsfc.nasa.gov>>. EUV flux density data in the range 0.1–165 nm stored at <[lasp.colorado.edu/home/see/data/](http://lasp.colorado.edu/home/see/data/)> are obtained from the SEE instrument onboard the TIMED satellite, which was at an average altitude of 625 km.

The National Center for Atmospheric Research, Colorado (NCAR) is acknowledged for making the TIE-GCM freely available at <<http://www.hao.ucar.edu/modeling/tgcm/tie.php>>. Mike Picone, Alan Hedin, and Doug Drob are thanked for sharing the NRLMSISE-00 model. Stanley Solomon from NCAR is thanked for providing valuable advice at various stages of this study. Sean Elvidge is thanked for sharing the code for the modified Taylor diagram.

## References

- Bennett, J., J. Sang, C. Smith, and K. Zhang (2015), An analysis of very short-arc orbit determination for low-earth objects using sparse optical and laser tracking data, *Advances in Space Research*, 55(2), 617–629.
- Bezděk, A. (2007), Lognormal distribution of the observed and modelled neutral thermospheric densities, *Studia Geophysica et Geodaetica*, 51(3), 461–468, doi:10.1007/s11200-007-0027-2.
- Bezděk, A., J. Sebera, and J. Klokočník (2017), Validation of Swarm accelerometer data by modelled nongravitational forces, *Advances in Space Research*, 59, 2512–2521, doi:10.1016/j.asr.2017.02.037.
- Chen, Y., L. Liu, and W. Wan (2011), Does the  $F_{10.7}$  index correctly describe solar EUV flux during the deep solar minimum of 2007–2009?, *Journal of Geophysical Research (Space Physics)*, 116, A04304.
- Codrescu, M. V., T. J. Fuller-Rowell, V. Munteanu, C. F. Minter, and G. H. Millward (2008), Validation of the coupled thermosphere ionosphere plasmasphere electrodynamics model: Ctipec-mass spectrometer incoherent scatter temperature comparison, *Space Weather*, 6(9), n/a–n/a, doi:10.1029/2007SW000364, s09005.
- Dickinson, R. E., E. C. Ridley, and R. G. Roble (1981), A three-dimensional general circulation model of the thermosphere, *Journal of Geophysical Research: Space Physics*, 86(A3), 1499–1512, doi:10.1029/JA086iA03p01499.
- Doornbos, E. (2012), *Thermospheric density and wind determination from satellite dynamics*, Springer, New York, USA.
- Drob, D. P., J. T. Emmert, G. Crowley, J. M. Picone, G. G. Shepherd, W. Skinner, P. Hays, R. J. Niciejewski, M. Larsen, C. Y. She, J. W. Meriwether, G. Hernandez, M. J. Jarvis, D. P. Sipler, C. A. Tepley, M. S. O'Brien, J. R. Bowman, Q. Wu, Y. Murayama, S. Kawamura, I. M. Reid, and R. A. Vincent (2008), An empirical model of the earth's horizontal wind fields: Hwm07, *Journal of Geophysical Research: Space Physics*, 113(A12), n/a–n/a, doi:10.1029/2008JA013668, a12304.
- Drob, D. P., J. T. Emmert, J. W. Meriwether, J. J. Makela, E. Doornbos, M. Conde, G. Hernandez, J. Noto, K. A. Zawdie, S. E. McDonald, J. D. Huba, and J. H. Klenzing (2015), An update to the horizontal wind model (hwm): The quiet time thermosphere, *Earth and Space Science*, 2(7), 301–319, doi:10.1002/2014EA000089, 2014EA000089.
- Elvidge, S., M. J. Angling, and B. Nava (2014), On the use of modified taylor diagrams to compare ionospheric assimilation models, *Radio Science*, 49(9), 737–745, doi:10.1002/

- 2014RS005435, 2014RS005435.
- Elvidge, S., H. C. Godinez, and M. J. Angling (2016), Improved forecasting of thermospheric densities using multi-model ensembles, *Geoscientific Model Development*, 9(6), 2279–2292, doi:10.5194/gmd-9-2279-2016.
- Emmert, J. T. (2015), Thermospheric mass density: A review, *Advances in Space Research*, 56, 773–824, <http://dx.doi.org/10.1016/j.asr.2015.05.038>.
- Emmert, J. T., S. E. McDonald, D. P. Drob, R. R. Meier, J. L. Lean, and J. M. Picone (2014), Attribution of interminima changes in the global thermosphere and ionosphere, *Journal of Geophysical Research: Space Physics*, 119(8), 6657–6688, doi:10.1002/2013JA019484, 2013JA019484.
- Friis-Christensen, E., H. Lühr, D. Knudsen, and R. Haagmans (2008), Swarm An Earth Observation Mission investigating Geospace, *Advances in Space Research*, 41, 210–216, doi:10.1016/j.asr.2006.10.008.
- Fuller-Rowell, T. J., and D. Rees (1980), A three-dimensional time-dependent global model of the thermosphere, *Journal of Atmospheric Sciences*, 37, 2545–2567, doi:10.1175/1520-0469(1980)037<2545:ATDTDG>2.0.CO;2.
- Hagan, M. E., M. D. Burrage, J. M. Forbes, J. Hackney, W. J. Randel, and X. Zhang (1999), Gswm-98: Results for migrating solar tides, *Journal of Geophysical Research: Space Physics*, 104(A4), 6813–6827, doi:10.1029/1998JA900125.
- Hathaway, D. H. (2015), The Solar Cycle, *Living Reviews in Solar Physics*, 12, 4, doi:10.1007/lrsp-2015-4.
- Hedin, A. E. (1987), MSIS-86 thermospheric model, *Journal of Geophysical Research*, 92, 4649–4662.
- Hedin, A. E., M. A. Biondi, R. G. Burnside, G. Hernandez, R. M. Johnson, T. L. Killeen, C. Mazaudier, J. W. Meriwether, J. E. Salah, R. J. Sica, R. W. Smith, N. W. Spencer, V. B. Wickwar, and T. S. Virdi (1991), Revised global model of thermosphere winds using satellite and ground-based observations, *Journal of Geophysical Research: Space Physics*, 96(A5), 7657–7688, doi:10.1029/91JA00251.
- Heelis, R. A., et al. (1982), A model of the high-latitude ionosphere convection pattern, *Journal of Geophysical Research*, 87(6339).
- Jones, M., J. T. Emmert, D. P. Drob, and D. E. Siskind (2017), Middle atmosphere dynamical sources of the semiannual oscillation in the thermosphere and ionosphere, *Geophysical Research Letters*, 44(1), 12–21, doi:10.1002/2016GL071741, 2016GL071741.
- Knipp, D. J., W. K. Tobiska, and B. A. Emery (2004), Direct and Indirect Thermospheric Heating Sources for Solar Cycles 21–23, *Sol Phys*, 224, 495–505, doi:10.1007/s11207-005-6393-4.
- Lin, C. S., et al. (2013), Satellite drag validation of the thermosphere-ionosphere electrodynamics general circulation model, *Tech. Rep. ADA587507*, Air Force Research Laboratory, NM, USA.
- Liu, H.-L. (2016), Variability and predictability of the space environment as related to lower atmosphere forcing, *Space Weather*, 14(9), 634–658, doi:10.1002/2016SW001450, 2016SW001450.
- Masutti, D., G. March, A. J. Ridley, and J. Thömel (2016), Effect of the solar activity variation on the global ionosphere thermosphere model (gitm), *Annales Geophysicae*, 34(9), 725–736, doi:10.5194/angeo-34-725-2016.
- Menvielle, M., and A. Berthelier (1991), The k-derived planetary indices: Description and availability, *Reviews of Geophysics*, 29(3), 415–432, doi:10.1029/91RG00994.
- Pedregosa, F., G. Varoquaux, A. Gramfort, V. Michel, B. Thirion, O. Grisel, M. Blondel, P. Prettenhofer, R. Weiss, V. Dubourg, J. Vanderplas, A. Passos, D. Cournapeau, M. Brucher, M. Perrot, and E. Duchesnay (2011), Scikit-learn: Machine learning in Python, *Journal of Machine Learning Research*, 12, 2825–2830.
- Picone, J. M., et al. (2002), NRLMSISE-00 empirical model of the atmosphere: Statistical comparisons and scientific issues, *Journal of Geophysical Research (Space Physics)*, 107, 1468.

- Qian, L., and S. C. Solomon (2012), Thermospheric density: An overview of temporal and spatial variations, *Space Science Reviews*, 168(1), 147–173, doi:10.1007/s11214-011-9810-z.
- Qian, L., et al. (2009), Seasonal variation of thermospheric density and composition, *Journal of Geophysical Research: Space Physics*, 114(A1), doi:10.1029/2008JA013643, a01312.
- Richards, P. G., J. A. Fennelly, and D. G. Torr (1994), EUVAC: A solar EUV flux model for aeronomic calculations, *Journal of Geophysical Research*, 99, 8981–8992, doi:10.1029/94JA00518.
- Richmond, A. D., E. C. Ridley, and R. G. Roble (1992), A thermosphere/ionosphere general circulation model with coupled electrodynamics, *Geophysical Research Letters*, 19, 601–604, doi:10.1029/92GL00401.
- Ridley, A. J., Y. Deng, and G. Tóth (2006), The global ionosphere thermosphere model, *Journal of Atmospheric and Solar-Terrestrial Physics*, 68, 839–864, <http://dx.doi.org/10.1016/j.jastp.2006.01.008>.
- Siemes, C., et al. (2016), Swarm accelerometer data processing from raw accelerations to thermospheric neutral densities, *Earth, Planets and Space*, 68(1), 1–16, doi:10.1186/s40623-016-0474-5, <http://dx.doi.org/10.1186/s40623-016-0474-5>.
- Siskind, D. E., D. P. Drob, K. F. Dymond, and J. P. McCormack (2014), Simulations of the effects of vertical transport on the thermosphere and ionosphere using two coupled models, *Journal of Geophysical Research: Space Physics*, 119(2), 1172–1185, doi:10.1002/2013JA019116.
- Solomon, S. C., and L. Qian (2005), Solar extreme-ultraviolet irradiance for general circulation models, *Journal of Geophysical Research: Space Physics*, 110(A10), n/a–n/a, doi:10.1029/2005JA011160, a10306.
- Solomon, S. C., L. Qian, L. V. Didkovsky, R. A. Viereck, and T. N. Woods (2011), Causes of low thermospheric density during the 2007–2009 solar minimum, *Journal of Geophysical Research: Space Physics*, 116(A2), n/a–n/a, doi:10.1029/2011JA016508, a00H07.
- Sutton, E. K., J. P. Thayer, W. Wang, S. C. Solomon, X. Liu, and B. T. Foster (2015), A self-consistent model of helium in the thermosphere, *Journal of Geophysical Research: Space Physics*, 120(8), 6884–6900, doi:10.1002/2015JA021223, 2015JA021223.
- Tapping, K. F. (2013), The 10.7-cm solar radio flux (f10.7), *Space Weather*, 11(7), 394–406, doi:10.1002/swe.20064.
- Taylor, K. E. (2001), Summarizing multiple aspects of model performance in a single diagram, *Journal of Geophysical Research: Atmospheres*, 106(D7), 7183–7192, doi:10.1029/2000JD900719.
- Vallado, D. A. (2004), *Fundamentals of astrodynamics and applications*, vol. 12, Space Technology Library, California, USA.
- Vallado, D. A., and D. Finkleman (2014), A critical assessment of satellite drag and atmospheric density modeling, *Acta Astronautica*, 95, 141–165.
- Walker, J. C. G. (1965), Analytic Representation of Upper Atmosphere Densities Based on Jacchia's Static Diffusion Models., *Journal of Atmospheric Sciences*, 22, 462–462, doi:10.1175/1520-0469(1965)022<0462:AROUAD>2.0.CO;2.
- Weimer, D. R. (2005), Predicting surface geomagnetic variations using ionospheric electrodynamic models, *Journal of Geophysical Research: Space Physics*, 110(A12), [A12307], <http://dx.doi.org/10.1029/2005JA011270>.
- Wu, Q., B. A. Emery, S. G. Shepherd, J. M. Ruohoniemi, N. A. Frisell, and J. Semeter (2015), High-latitude thermospheric wind observations and simulations with superdarn data driven near tiegcm during the december 2006 magnetic storm, *Journal of Geophysical Research: Space Physics*, 120(7), 6021–6028, doi:10.1002/2015JA021026, 2015JA021026.
- Xiong, C., C. Stolle, and H. L  ijhr (2016), The swarm satellite loss of gps signal and its relation to ionospheric plasma irregularities, *Space Weather*, 14(8), 563–577, doi:10.1002/2016SW001439, 2016SW001439.

Zesta, E., and C. Huang (2016), *Satellite Orbital Drag*, pp. 329–347, CRC Press, Boca Raton, FL, USA, doi:10.1201/9781315368474-19.